Deep Neural Network-Based Sinogram Super-Resolution and Bandwidth Enhancement for Limited-Data Photoacoustic Tomography

Navchetan Awasthi, Gaurav Jain, *Student Member, IEEE*, Sandeep Kumar Kalva, Manojit Pramanik, and Phaneendra K. Yalavarthy, *Senior Member, IEEE*

***Abstract*— Photoacoustic tomography (PAT) is a noninvasive imaging modality combining the benefits of optical contrast at ultrasonic resolution. Analytical reconstruction algorithms for photoacoustic (PA) signals require a large number of data points for accurate image reconstruction. However, in practical scenarios, data are collected using the limited number of transducers along with data being often corrupted with noise resulting in only qualitative images. Furthermore, the collected boundary data are band-limited due to limited bandwidth (BW) of the transducer, making the PA imaging with limited data being qualitative. In this work, a deep neural network-based model with loss function being scaled root-mean-squared error was proposed for super-resolution, denoising, as well as BW enhancement of the PA signals collected at the boundary of the domain. The proposed network has been compared with traditional as well as other popular deep-learning methods in numerical as well as experimental cases and is shown to improve the collected boundary data, in turn, providing superior quality reconstructed PA image. The improvement obtained in the Pearson correlation, structural similarity index metric, and root-mean-square error was as high as 35.62%, 33.81%, and 41.07%, respectively, for phantom cases and signal-to-noise ratio improvement in the reconstructed PA images was as high as 11.65 dB for *in vivo* cases compared with reconstructed image obtained using original limited BW data. Code is available at https://sites.google.com/site/sercmig/home/dnnpat.**

***Index Terms*— Bandwidth (BW) enhancement, convolutional neural networks, image reconstruction, photoacoustic (PA) imaging, super-resolution.**

I. Introduction

PHOTOACOUSTIC tomography (PAT), also referred to as optoacoustic tomography is an "imaging from coupled physics", has revolutionized biomedical imaging by facilitating high optical contrast along with high spatial resolution [1], [2]. Over the years, PAT has emerged as a noninvasive hybrid imaging modality, effectively unifying the merits of optical excitation and ultrasonic detection facilitating higher imaging depths [3]–[8]. In PAT, the tissue under investigation is irradiated with a nanosecond short laser pulse in the near-infrared (NIR) region. The NIR characteristics, such as low absorption and scattering coefficient in biological tissues, result in deep tissue penetration achieving increased signal-to-noise ratio (SNR) without damaging the tissue. Light energy incident on the tissue is partially absorbed by it, consequently increasing the temperature due to thermoelastic expansion resulting in the emission of acoustic waves. Subsequently, the generated waves propagate across the biological tissue and are detected by wideband ultrasound transducers located at the tissue boundary. Using reconstruction algorithms, information acquired by these transducers gets utilized to compute the initial pressure rise, which is proportional to the absorbed optical (or ultrasonic) energy. In addition, the optical absorption coefficient is highly susceptible to the pathophysiology of the tissue, enabling PAT to distinguish the pathophysiological nature of the tissue in high contrast with ease (assuming homogeneous fluence). Hence, photoacoustic (PA) imaging unravels functional and structural information in a scalable manner, which further amplifies its utility for both clinical and preclinical applications [6], [9].

The most important part of PA imaging is to reconstruct accurate PA images using the acquired PA signals. For this, the acoustic inverse problem needs to be solved to estimate the initial pressure at time $t = 0$ using the acoustic measurements acquired through the transducers at time t. Several reconstruction algorithms exist in the literature, which can be broadly classified into: 1) analytical methods and 2) model-based iterative methods [10]–[13]. Based on the spherical radon transform model, analytical methods, such as filtered backprojection (BP), delay & sum,

Manuscript received January 3, 2020; accepted February 23, 2020. Date of publication February 28, 2020; date of current version November 23, 2020. The work was supported by DST-ICPS cluster funding (T-851) for the data science program as well as through IFTAS-CDS Collaborative Laboratory of Data Science and Engineering. *(Navchetan Awasthi and Gaurav Jain contributed equally to this work.) (Corresponding author: Phaneendra K. Yalavarthy.)*

Navchetan Awasthi is with the Department of Computational and Data Sciences, Indian Institute of Science, Bengaluru 560012, India, also with the Massachusetts General Hospital, Boston, MA 02114 USA, and also with Harvard University, Cambridge, MA 02138 USA (e-mail: navchetana@iisc.ac.in).

Gaurav Jain is with the Department of Computational and Data Sciences, Indian Institute of Science, Bengaluru 560012, India, and also with the Department of Computer Science and Engineering, Delhi Technological University, New Delhi 110042, India (e-mail: gauravjain13298@gmail.com).

Sandeep Kumar Kalva is with the School of Chemical and Biomedical Engineering, Nanyang Technological University, Singapore 637459, and also with the University of Zurich, 8006 Zürich, Switzerland (e-mail: sandeepk002@e.ntu.edu.sg).

Manojit Pramanik is with the School of Chemical and Biomedical Engineering, Nanyang Technological University, Singapore 637459 (e-mail: manojit@ntu.edu.sg).

Phaneendra K. Yalavarthy is with the Department of Computational and Data Sciences, Indian Institute of Science, Bengaluru 560012, India (e-mail: yalavarthy@iisc.ac.in).

Digital Object Identifier 10.1109/TUFFC.2020.2977210

and the Fourier transform-based methods, as well as model-based time-reversal methods although computationally frugal, require massive amounts of data for accurate image reconstruction. Large data requirements commensurate with increased scan time and excessive experimental setup cost, rendering it practically infeasible to meet such huge data requirements. Also, the limited aperture of transducers further prohibits the data collection. Hence, analytical methods in these limited-data scenarios result in qualitative imaging [14]–[16]. On the other hand, model-based iterative models perform considerably better than their analytical counterparts in context to limited data and display robustness to noise. However, these methods are computationally expensive and have high memory constraints. Hence, due to the setup cost and practical considerations, the reconstruction of PA images is a challenging task, given the limited data and memory restrictions for real-time applications. Irrespective of the reconstruction algorithm employed, factors such as SNR, quality of PA signals, and limited bandwidth (BW) of the ultrasound transducers affect the performance of these techniques. For any pragmatic experimental setting, transducers are always band-limited and introduce a blurring effect on the reconstructed images.

In order to overcome the inevitable limitation arising due to band-limited ultrasound transducers, an additional step is required to reinstate the quality of reconstructed PA images. Earlier, a deconvolution-based deblurring algorithm was proposed by Rejesh *et al.* [17]. In this approach, the detected PA signal is convolved with a transducer impulse response to restore the original PA signal. However, deconvolution-based approaches have been classified as "ill-posed" [18] due to their failure to achieving unique solutions when the data are approximate and, thereby, entail regularization. Cao *et al.* [19] recently proposed an inverse filtering method coupled with multisampled signal denoising technique to recover out-of-band frequency components. This signal recovery not only resulted in increased SNR but also managed to reveal deeper structural details in reconstructed PA images.

Over the past few years, deep learning has been extensively employed in the biomedical imaging domain, outperforming most of the existing classical approaches. In particular, convolutional neural networks have witnessed proliferation in application to computer-aided detection [20]–[23], segmentation [24]–[27], and image reconstruction [28]–[31]. Antholzer *et al.* [32] proposed a method for improving the quality of the reconstructed PA images obtained using the BP technique via a deep-learning-based architecture. Reiter and Bell [33] and Allman *et al.* [34] introduced a convolutional neural network that was trained to identify the location of the individual point targets for PA imaging, without requiring traditional geometry-based beamforming from the beamformed data for various sound speeds, target locations, and absorber sizes. In [35], a deep neural network was proposed for providing high-resolution 3-D PA images from the limited view data. The model represented an iterative scheme and incorporates gradient information of the data for compensating the limited view artifacts. Davoudi *et al.* [36] proposed a U-Net-based deep neural network for getting superior quality PA images to form the substantially undersampled data or limited view scans.

In this article, a hybrid end-to-end trainable deep neural network model was proposed for super-resolution, denoising, as well as BW enhancement of PA signals for the effective reconstruction of quantitatively accurate PA images. Furthermore, the proposed approach may be applied to ultrasound tomography, tweaking the parameters and fine-tuning the model. The super-resolution-based techniques using simple convolutional neural networks and U-Net-based architectures have been used in computed tomography (CT) [37], [38] and currently have not been used in PAT. There have been different architectures used for super-resolution, such as VDSR [39] (accurate image super-resolution using very deep convolutional networks) that uses high learning rate and residual learning, RED30 [40] (image restoration using very deep convolutional encoder–decoder networks with symmetric skip connections) that symmetrically links convolutional and deconvolutional layers with skip-layer connections and training loss converges much faster and attains a higher quality local optimum, deeply recursive convolutional network (DRCN) for image super-resolution [41] that uses recursive supervision and skip connection, super-resolution generative adversarial networks (SR-GANs) [42] that use a perceptual loss function consisting of an adversarial loss, and a content loss to recover photorealistic textures from heavily downsampled images on public benchmarks. These architectures have been used for super-resolution of natural images, whereas the U-net that was utilized in this work was shown to perform well on medical images [38], and hence, these architectures were not utilized. In PAT, there have been different deep-learning architectures that were used for improving back projection-based reconstruction, the fusion of different reconstruction techniques [43], but there has not been any work in the sinogram (data) domain to perform the super-resolution and BW enhancement using a simple network. The BW enhancement using neural networks was attempted earlier, and it has shown limited improvement [44]. This is the first network that proposes super-resolution (increasing the available data), denoising, as well as BW enhancement of collected PA data for improving PAT. The main contributions of the work can be summarized as follows.

1) It is the first kind of single network that performs super-resolution, denoising, as well as the BW enhancement of PA data in the sinogram domain (the majority of deep-learning networks have been proposed in the image space, i.e., improve the reconstructed image).
2) The proposed neural network works on the full sinogram, rather than at pixel-level, thus inherently providing robustness and generalization. The robustness was also shown when the network was trained for numerical phantoms and was shown to perform well even for experimental *in vivo* data.
3) The architecture proposed with modifications can be used to enhance the experimentally collected raw data (sinogram), which can, in turn, improve the outcome of an inverse problem, thus inherently removing the bias of the image reconstruction method.
4) Introduction of the scaled root-mean-square loss function for training the network for sinogram data, which contains values with extremely low magnitude, can be

extended to other applications that share properties of PA data. The scaling also helps in preserving the gradient values with small magnitudes, and thus, the vanishing gradient problem can be solved.

5) The method is shown to perform favorably as compared with the other state-of-the-art conventional and deep-learning-based techniques, such as automated wavelet denoising (AWD), super-resolution convolutional neural network (SRCNN), and U-net architectures.
6) The PA data generated through k-WAVE MATLAB Toolbox for training the model were made publicly available to augment research in PA imaging, encouraging the community to develop methods that can improve the sinogram (rather than doing it indirectly by improving the reconstructed image).

The rest of this article is organized as follows. In Section II, we briefly introduce existing methods and elucidate the proposed method. In Section III, evaluation metrics have been discussed, whereas in Section IV, details about the experimental setup have been canvassed. Section V validates the performance of the proposed approach.

II. Photoacoustic Image Reconstruction

In this section, the PA image reconstruction along with few approaches to overcome its limitations is being discussed. A detailed explanation of the proposed deep-learning-based approach is given in the following.

A. Forward Problem

In PAT, the forward model provides the computation of data collected by acoustic transducers located at the tissue boundary using (1), which determines the propagation and generation of the acoustic wave inside the tissue [8]

$$\left(\Delta^2 - \frac{1}{c^2}\frac{\partial^2}{\partial t^2}\right)\mathcal{P}(\vec{x}, t) = \frac{-\alpha}{\mathcal{C}_p}\frac{\partial \mathcal{H}(\vec{x}, t)}{\partial t} \tag{1}$$

where $\mathcal{P}(\vec{x}, t)$ represents the PA wave pressure at location $\vec{x}$ at time t, c is the speed of light, $\mathcal{C}_p$ denotes the specific heat capacity, α represents the coefficient of thermal expansion, and $\mathcal{H}(\vec{x}, t)$ represents the energy deposited per unit volume per unit time. Furthermore, the reconstruction/inverse problem incorporates estimating the initial pressure $\mathcal{P}(\vec{x}, t = 0)$ given the acquired boundary measurements at time t, making it an initial value problem. Section II-B describes the system of equations governing the numerical experimental setup.

B. System Matrix Building

In order to simplify the PA wave propagation model, it can be represented through a linear system of equations as follows:

$$\mathbf{A}x = b \tag{2}$$

where $\mathbf{A} \in \mathbb{R}^{m \times n^2}$ is the system matrix containing impulse responses such that each column represents the response of a pixel in the imaging domain for varying time domains. Here, m is the product of the number of transducers and the number of time samples that each of these transducers acquires, and x denotes an image of size $n \times n$ pixels, which is converted to a vector such that $x \in \mathbb{R}^{n^2 \times 1}$. The data collected by each transducer, i.e., $b \in \mathbb{R}^{m \times 1}$, are computed using (2) in the simplified forward model [45], [46]. To obtain the image, linear BP (LBP) method can be used as [47]

$$x_{\text{LBP}} = \mathbf{A}^{\mathcal{T}} b \tag{3}$$

where $x_{\text{LBP}} \in \mathbb{R}^{n^2 \times 1}$ is the image vector and $\mathbf{A}^{\mathcal{T}}$ is the transpose of the system matrix. The LBP method is one of the most basic methods for image reconstruction. In this work, the image reconstruction was performed using the LBP method due to its low computation time and being analytical in nature. Since the sinogram has been improved using the proposed deep neural network, the LBP will be effective in comparison to reconstructed results as it does not have any parameters (such as regularization) that affect the image quality. In the experiments explained in this work, the same setup as comprehensively explained in [45] and [46] was employed. Section II-C describes an automated wavelet-based denoising method to improve boundary data, in turn, improving the reconstructed PA images.

C. Automated Wavelet Denoising Method

The data obtained using the interpolation can be denoised using the maximum overlap DWT (MODWT) [48] method (nonorthogonal transform) using the wavelet denoising [49]. The advantages of MODWT are as follows.

1) The sample size is not restricted to powers of 2.
2) Zero padding is not required.
3) It forms a zero-phase filter and, hence, lines up with the features of the original signal in contrast to the DWT transform.

The complete discussion can be found in [48] for interested readers. The application to PA images has been discussed in [49]. In this work, MODWT has been utilized for denoising the PA signals obtained after interpolation of the data obtained using 100 detectors. The threshold for denoising is chosen by the universal threshold criteria [50].

D. Super-Resolution Convolutional Neural Network

Image super-resolution [51] has a wide application to translate an image from a low-resolution to a high-resolution image. Previous techniques exploit internal similarities of the same image [52]–[54] or learn mapping functions [55]–[57] for translation of a low-resolution to high-resolution image. These techniques are challenged by difficulties in effectively and compactly modeling the data. Sparse coding techniques [58], [59] were used in the past for image-based super-resolution. It involves the extraction of overlapping patches, encoded by a low-resolution dictionary. These coefficients are then used for constructing the dictionary, which helps to build a corresponding high-resolution image. These techniques either learn and optimize dictionaries [58], [59] or try to model them in different ways [55], [56]. SRCNN [60] was utilized to model one such dictionary that learns the mapping from a low-resolution to high-resolution image. This architecture was used to first map the noisy, band-limited patches using 100 detectors to noiseless, full BW patches using

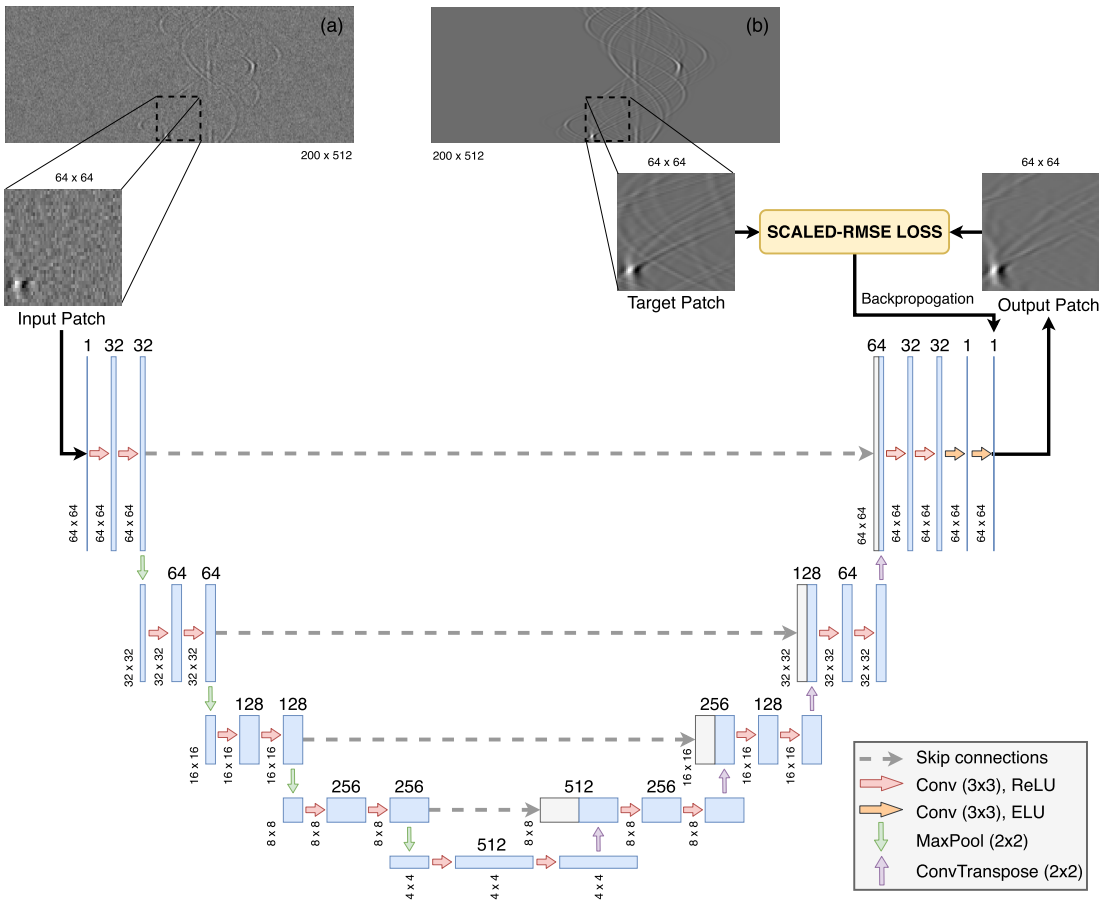

Fig. 1. Training configuration for the proposed U-Net-based architecture. (a) Data collected through 100 transducers with 70% BW are added with variable noise resulting in SNR values of data from 10 to 70 dB. Patches of size 64 × 64 are cropped from (a) and input into the U-Net-based model. (b) Output patch of size 64 × 64 is then used to compute the scaled-RMSE loss with the corresponding patch from the data collected through 200 transducers and 100% BW. This loss is propagated backward to train the proposed model for BW enhancement, super-resolution, and denoising.

200 detectors. For comparing the performance of SRCNN with the proposed network, the implementation configurations mentioned in the original work [60] were deployed.

E. Proposed Method

Deep learning has found numerous applications in image processing tasks, such as image enhancement, edge detection, and image super-resolution. These have been recently extended to applications in CT imaging for super-resolution of the sinogram data using simple convolutional layers as well as an U-Net-based architecture [38]. In this work, a hybrid end-to-end trainable U-Net-based model [61] is proposed for super-resolution, denoising, as well as BW enhancement of PA signals. Sections II-E1–II-E3 discuss the architecture, training details, and testing methodology for the proposed.

1) Architecture: The proposed method trains an U-Net-based architecture shown in Fig. 1. The first layer contains 32 convolutional filters of size 3 × 3 with a stride of 2 × 2, which progressively increases in powers of 2 until the bottleneck layer with a maximum of 512 filters. Each layer with the corresponding number of 3 × 3 filters applies two consecutive convolution operations with rectified linear unit (RELU) activations followed by a max-pooling layer with a window of size 2 × 2. In [38], pooling layers were utilized for super-resolving the sinogram data of CT images. The pooling layer that was utilized in this work downsamples the input using max-pooling (similar to [38]). It helps in making shift-invariant results by taking only specific values for the input. It also reduces the spatial size of representation and the number of parameters and computation in the network. The shift invariance plays an important role in image segmentation and image classification where the position of the target is arbitrary. After downsampling the input to reach the bottleneck layer, symmetrically inverse operations were applied using the same filter size and stride to upsample the bottleneck layer to obtain an output of the same size as the input. The number of filters decreases progressively over the layers in a symmetric fashion. At each layer, zero padding of size "1" was performed to maintain the size before and after convolution operations. Skip connections were added during upsampling from the corresponding downsampled layers in order to maintain the overall sinogram structure, as shown in Fig. 1. Note that the original U-Net architecture layers employ softmax activation functions in the final two layers for segmentation. However, we used exponential linear unit (ELU) [see (5)] activation [62]. Although RELUs have been employed extensively for modeling images or improving the reconstruction quality through deep neural networks, it fails to effectively characterize PA data that contain positive as well as negative values. Hence, in this work, ELU activations

were employed, which have been shown to outperform RELU activations for specific tasks [62]. The motivation for this stems from the fact that sinogram data may contain negative values, in which the RELU activations fail to achieve as evident from (4)

$$\text{relu}(x) = \begin{cases} x, & \text{if } x > 0 \\ 0, & \text{if } x \leq 0 \end{cases} \tag{4}$$

$$\text{elu}(x) = \begin{cases} x, & \text{if } x > 0 \\ \alpha(e^x - 1), & \text{if } x \leq 0 \end{cases} \tag{5}$$

where x is the input and α is the regularization parameter for elu. In addition to this, ELUs push the mean unit activations to zero, thereby mimicking batch normalization with an advantage of lower computational complexity. To further evaluate this, we compare three variants of the U-Net architecture: 1) U-Net (Relu) where all activations are ReLUs; 2) U-Net (Elu) where all activations are ELUs; and (3) U-Net (Hybrid) where ELUs have only been used in the final layers. The proposed U-Net (Hybrid) variant was able to provide the generalization by effectively modeling the negative values in sinogram through the final layers while maintaining the advantages of ReLUs in U-Net architecture.

2) Training: For training the proposed model for super-resolution and BW enhancement of the sinogram domain data, training data were generated using k-WAVE MATLAB toolbox, as mentioned in Section IV. Sinogram data obtained corresponding 1000 breast images [63] were used to train the model. Sinogram was generated for all these images for limited BW for 100 detectors and full BW for 200 detectors for training the network. The sinogram data were obtained using the limited BW detectors placed at the boundary of the imaging domain. These sinograms obtained were then added with the Gaussian noise, and the sampled noisy sinograms were used as the input for the network. The output consists of fully sampled, full BW, and denoised sinograms. Since these output sinograms correspond to at least 200 detectors data and do not contain noise, the reconstruction of the PA image was performed via LBP [47] technique. Note that the aim of this work is to show that the proposed network is capable of enhancing the PA data (sinogram), so the utilization of simple BP as the reconstruction method does provide unbiased way of quantifying the improvement of image quality. Reconstructed image quality using filtered back projection or other variants [64] depends on the choice of appropriate filter or parameters in the filter, which may not be straightforward to assess the improvement in the PA data obtained via the methods discussed here. From each image, 105 patches of size 64×64 were generated by sliding over the 200×512 sinogram data with a stride of 16×16. A total of $105 \times 1000 = 105\,000$ patches were used for training, where a 20% split for training and validation was done. The training data set has 84 000 patches, while the validation data set has 21 000 patches. Furthermore, the Gaussian noise in the range of 10–70 dB was added in the data, while the training and ground truth were the patches generated using the 200 detectors data. The total number of trainable parameters used for training the network was 7 759 787. The network

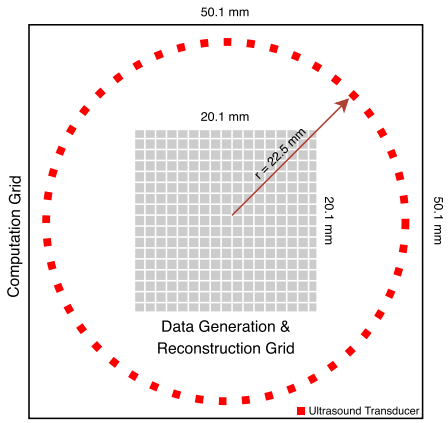

Fig. 2. Illustrative representation of the data collection setup. Computational grid of 501×501 with an array of 200 ultrasound transducers around the data generation grid of 401×401 and a 201×201 pixels reconstruction grid is shown. Transducers are placed at a radial distance of 22.5 mm from the center of the grid setup.

was trained using the proposed scaled root-mean-square error (scaled-RMSE) loss function, defined as

$$\mathcal{L} = \frac{1}{N} \sum_{i=1}^{N} \|\hat{x}_i - \phi(x_i)\|^2 \times \tau \tag{6}$$

where $\hat{x}_i$ is the predictions of the model and $\phi(x_i)$ is the true signals. Since sinogram data contain values of the order of 0.0001, a loss multiplication factor, $\tau = 10\,000$ was used to ensure effective backpropagation of the loss to the initial layers. It enables us to train a deeper network without worrying about the dying out of loss gradients and hence preventing the problem of vanishing gradients. In [65], loss scaling was proposed to preserve gradient values with small magnitudes. It was shown that scaling up the gradients will shift them to occupy more of the representable range and, hence, will result in preserving values that are otherwise close to zero. One of the approaches of scaling is to scale the loss obtained in the forward pass before starting the computation of backpropagation. Once scaling is performed, chain rule affects all the computed values by the same amount, and thus, no extra operations are required, and the vanishing gradient problem can be easily avoided. The scaling factor was determined after extensive experimentation, and the optimal value of 10 000 was obtained for the proposed method utilizing the approach mentioned in [65]. The scaling of the input by the factor has not been tried in the proposed method as the input data need to be multiplied by the same factor, while in case of loss scaling, it will be only one multiplication. Furthermore, the Adam optimizer was used for training the network with $\gamma = 0.98$ with a step size of 2. The learning rate, the number of epochs, and the batch size were set to be 1e-3, 250, and 128, respectively. The model was fine-tuned to obtain the best set of hyper-parameters, such as the starting number of filters (32), the maximum number of filters (512), batch size, learning rate, γ, step size, and epochs. All computations were carried out on a Linux workstation with Intel Xeon Silver 4110 CPU with 2.10-GHz clock speed, having 128-GB RAM and a TITAN RTX GPU with 24-GB memory. It took 65 s (approximately) for one epoch, and

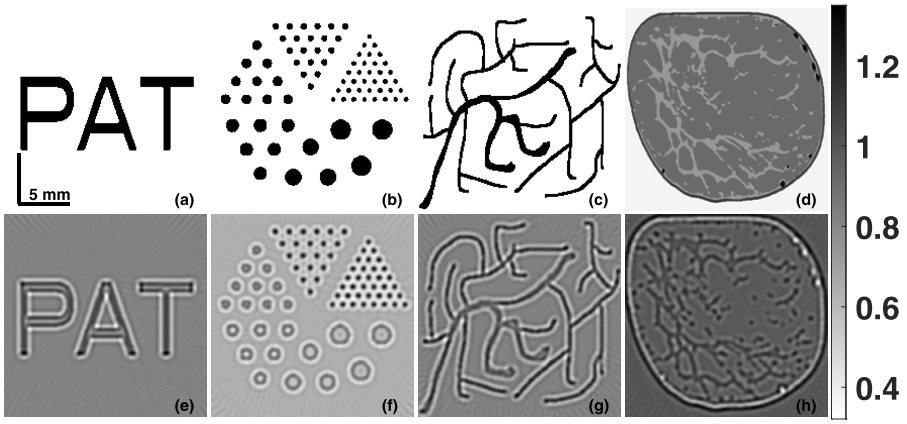

Fig. 3. Target numerical phantoms used for quantitative evaluation of the proposed method. (a)–(d) Ground-truth images for PAT, modified Derenzo, BV, and breast phantoms. Corresponding reconstructed images using LBP with full BW and noise less data are shown in (e)–(h) to serve as reference for best case.

a total of 4.5 h (approximately) to train the model using the above-mentioned workstation. PyTorch implementation of the proposed method shall be made available online at https://sites.google.com/site/sercmig/home/dnnpat.

3) Testing: For testing, input data obtained using limited BW (70% for numerical data) and low resolution, i.e., 100 detector data, were first interpolated using nearest neighbor to obtain a sinogram of size 200×512. This sinogram data were padded using the "reflect" padding to obtain a sinogram data of size 512×512. This was performed to ensure that there is no mismatch between the tensor sizes while concatenating the skip connections. The padded sinogram data are input into the model to obtain super-resolved sinogram data with full BW. This enhanced data were then reconstructed using BP to obtain reconstructed PA images. These images are then evaluated using the figure of merits to analyze the improvement observed with the proposed method. Section III discusses the figures of merit used for evaluation.

III. Figures of Merit

Quantitative performance of the proposed method has been compared with existing state-of-the-art methods over the reconstructed PA images using evaluation metrics, namely, RMSE, structural similarity (SSIM) index, Pearson correlation (PC), and SNR. For numerical phantoms, RMSE, PC, and SSIM were compared, whereas for experimental *in vivo* phantoms, SNR was employed as the sole criterion of evaluation due to the absence of target initial pressure. The following describes the metrics in detail.

A. Root-Mean-Square Error

The RMSE evaluates the standard deviation of the residuals as an absolute measure to evaluate the quality of the reconstructed image [66], [67], defined as

$$\mathrm{RMSE}(\mathcal{I}^{\mathrm{target}}, \mathcal{I}^{\mathrm{rec}^n}) = \sqrt{\frac{\sum_{i,j}^{\mathcal{N}} \left(\mathcal{I}_{i,j}^{\mathrm{target}} - \mathcal{I}_{i,j}^{\mathrm{rec}^n}\right)^2}{\mathcal{N}^2}} \tag{7}$$

where $\mathcal{I}^{\mathrm{target}}$ and $\mathcal{I}^{\mathrm{rec}^n}$ denote the target and reconstructed images, each of pixel size $\mathcal{N} \times \mathcal{N}$. Lower residuals are ideal for a good quality reconstructed images, and hence, low-RMSE values are desirable.

B. Structural Similarity Index

SSIM amalgamates three comparative measurements, namely, luminance (l), contrast (c), and structure/ correlation(s) to evaluate the quality of an image with respect to a reference image. In our case, similarity of the reconstructed image (rec^n) is computed with respect to the target image [68], [69]. The three parameters are defined as

$$l(\mathrm{target}, \mathrm{rec}^n) = \frac{2\mu_{\mathrm{target}}\mu_{\mathrm{rec}^n} + c_1}{\mu_{\mathrm{target}}^2 + \mu_{\mathrm{rec}^n}^2 + c_1} \tag{8}$$

$$c(\mathrm{target}, \mathrm{rec}^n) = \frac{2\sigma_{\mathrm{target}}\sigma_{\mathrm{rec}^n} + c_2}{\sigma_{\mathrm{target}}^2 + \sigma_{\mathrm{rec}^n}^2 + c_2} \tag{9}$$

$$s(\mathrm{target}, \mathrm{rec}^n) = \frac{\sigma_{\mathrm{target},\mathrm{rec}^n} + c_3}{\sigma_{\mathrm{target}}\sigma_{\mathrm{rec}^n} + c_3} \tag{10}$$

where μ_{target} and μ_{rec^n} represent the mean, σ_{target} and σ_{rec^n} represent the variance of the target and reconstructed images, respectively, $\sigma_{\mathrm{target},\mathrm{rec}^n}$ represents the covariance between the two images, and c_1, c_2, and c_3 are constants such that $c_3 = c_2/2$. SSIM is defined as the weighted combination of the three components, $\mathrm{SSIM} = [l^\alpha \cdot c^\beta \cdot s^\gamma]$. Higher the SSIM, higher the similarity between the reconstructed and target image.

C. Pearson Correlation

Pearson Correlation is a measure of linear correlation between two entities [70]. Here, correlation between the target image $\mathcal{I}^{\mathrm{target}}$ and reconstructed image $\mathcal{I}^{\mathrm{rec}^n}$ is computed as

$$\mathrm{PC}(\mathcal{I}^{\mathrm{target}}, \mathcal{I}^{\mathrm{rec}^n}) = \frac{\mathrm{cov}(\mathcal{I}^{\mathrm{target}}, \mathcal{I}^{\mathrm{rec}^n})}{\sigma(\mathcal{I}^{\mathrm{target}}) \cdot \sigma(\mathcal{I}^{\mathrm{rec}^n})} \tag{11}$$

where cov represents the covariance and σ represents the variance. $\mathrm{PC} \in [-1, 1]$, where 1 denotes complete linear correlation, 0 represents no linear correlation, and -1 indicates a perfectly complementary relationship.

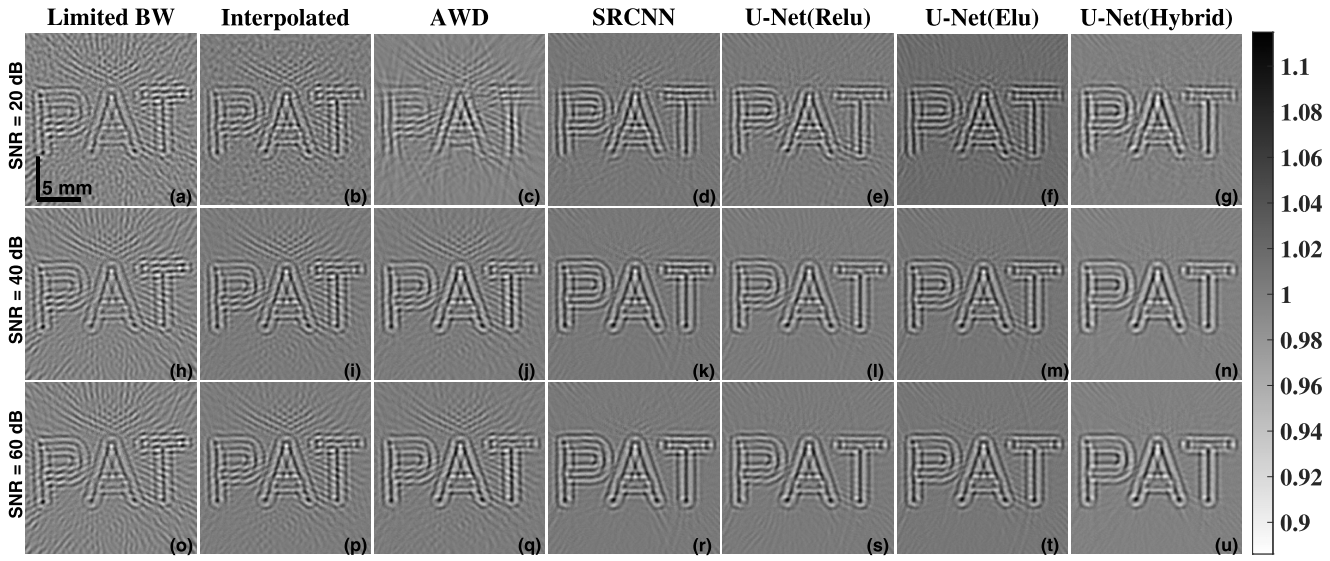

Fig. 4. Reconstructed PAT phantom images with each row representing the SNR of data being 20, 40, and 60 dB and correspondingly given in (a)–(g), (h)–(n), and (o)–(u), respectively. Reconstructed images using data with limited BW (70%) and 100 transducers are shown in (a), (h), and (o). While (b), (i), and (p) show reconstruction results when the data with 100 transducers that are interpolated using nearest neighbor to obtain a 200 transducer data. (c), (j), and (q) Results obtained using the automated wavelet denoising approach. The results obtained using the SRCNN-based method are shown in (d), (k), and (r), and the results obtained using the U-Net (Relu) are shown in (e), (l), and (s). Finally, (f), (m), and (t) show the results obtained using the proposed U-Net (Elu) approach, and (g), (n), and (u) show the results obtained using the proposed U-Net (Hybrid)-based approach. Table I reports the figure of merits of these results in a comparative manner.

D. Signal-to-Noise Ratio

SNR is a quantitative measure that assesses the desired signal strength in comparison with the background noise [71]. As mentioned earlier, the target initial pressure distribution is unavailable for experimental *in vivo* phantoms; hence, SNR is employed to analyze the quantitative improvement. It is defined as

$$\text{SNR}_r\ (\text{dB}) = 20 \times \log_{10}\left(\frac{\mathcal{S}}{\sigma_{\text{noise}}}\right) \tag{12}$$

where $\mathcal{S}$ represents the signal power and σ_{noise} represents the standard deviation in the noise. A higher SNR value (in dB) is desired in the reconstructed PA image.

IV. Numerical and Experimental Studies

This section describes the numerical and experimental setup for generating data similar to as done in [43], [46], and [72]. A computational grid of 501 × 501 pixels was employed with 0.1 mm/pixel. For data generation, a high-dimensional 401 × 401 pixels grid was used, while reconstruction was performed on a low-dimensional grid of 201 × 201 pixels to avoid the inverse problem. The white Gaussian noise was added to the data generated in order to achieve variable noise levels having SNR values between 20 and 60 dB. As shown in Fig. 2, 100 point transducers with a BW of 70% having central frequency of 2.25 MHz were placed at the tissue boundary in a circularly equidistant manner at a radius of 22.5 mm. Each transducer sampled 512 observations after every 500 ms, i.e., a sampling frequency of 20 MHz. Speed of sound in the medium (tissue under investigation) was assumed to be a uniform with no absorption or dispersion at 1500 m/s. This configuration results in a system matrix $\mathbf{A} \in \mathbb{R}^{51\,200\times 40\,401}$.

For a comprehensive comparison of the proposed method with existing approaches, four distinct numerical phantoms, namely, PAT, modified Derenzo, blood vessel (BV), and breast, were considered. The numerical experimental data were generated using the open-source k-WAVE MATLAB toolbox [73]. The PAT phantom constitutes the alphabets "PAT" [see Fig. 3(a)] and aids in determining the efficacy of recovering sharp objects. The modified Derenzo phantom [see Fig. 3(b)] contains circular object groups with differing radii that assist in evaluating the recovery strength of small and large objects. The BV phantom [see Fig. 3(c)], as the name suggests, resembles the thick and thin BV-like structures and help analyze the success in the recovery of amorphous complicated structures. Note that a maximum initial pressure distribution of 1 kPa was asserted for the first three phantoms. Finally, the breast phantom was created using contrast-enhanced imaging data [63], [74]. In this phantom, the initial pressure was varied from 0 to 5 kPa, and the expected initial pressure distribution was given in Fig. 3(d). Breast phantoms help in testing the robustness of the proposed approach in cases with complex PA images bearing variable contrast and noise. The reconstructed images using noiseless data with 200 detectors using these four phantoms were presented in the second row of Fig. 3 to serve as a reference (to know what is truly achievable).

In addition, performance of the proposed approach is evaluated using two experimental phantoms: 1) horse-hair phantom (see Fig. 8) and 2) *in vivo* rat-brain phantom (see Fig. 9). The trilateral horse-hair phantom data were acquired using Nd:YAG laser, while the *in vivo* rat-brain phantom data were acquired using a pulsed laser diode (PLD). Furthermore, we restrict ourselves with any detailed description of the

TABLE I
COMPARATIVE RESULTS OBTAINED FOR THE RECONSTRUCTED PAT PHANTOM IMAGES SHOWN IN FIG. 4 IN TERMS OF FIGURE OF MERITS: PC COEFFICIENT, SSIM INDEX, AND RMSE FOR SNR OF DATA BEING 20, 40, AND 60 dB. BOLD TEXT INDICATES THE BEST POSSIBLE VALUE FOR THE METRIC USED

SNR of data	20 dB			40 dB			60 dB		
Method/ Metric	PC	SSIM	RMSE	PC	SSIM	RMSE	PC	SSIM	RMSE
Limited BW	0.3077	0.2728	0.1078	0.3293	0.3262	0.1012	0.3293	0.3262	0.1012
Interpolated	0.5317	0.4386	0.0871	0.5738	0.5417	0.0822	0.5746	0.5429	0.0805
Automated Wavelet Denoising	0.5387	0.5376	0.0782	0.6367	0.5761	0.0765	0.6367	0.5761	0.0765
SRCNN	0.6712	0.6474	0.0806	0.7375	0.7096	0.0711	0.7386	0.7100	0.0685
U-Net (Relu)	0.6668	0.6416	0.0756	0.7396	0.7289	0.0637	0.7421	0.7291	0.0642
U-Net (Elu)	0.6676	0.6501	0.1083	0.7388	0.7201	0.0754	0.7419	0.7228	0.0721
U-Net (Hybrid)	**0.7306**	**0.7034**	**0.0617**	**0.7721**	**0.7709**	**0.0539**	**0.7727**	**0.7704**	**0.0539**

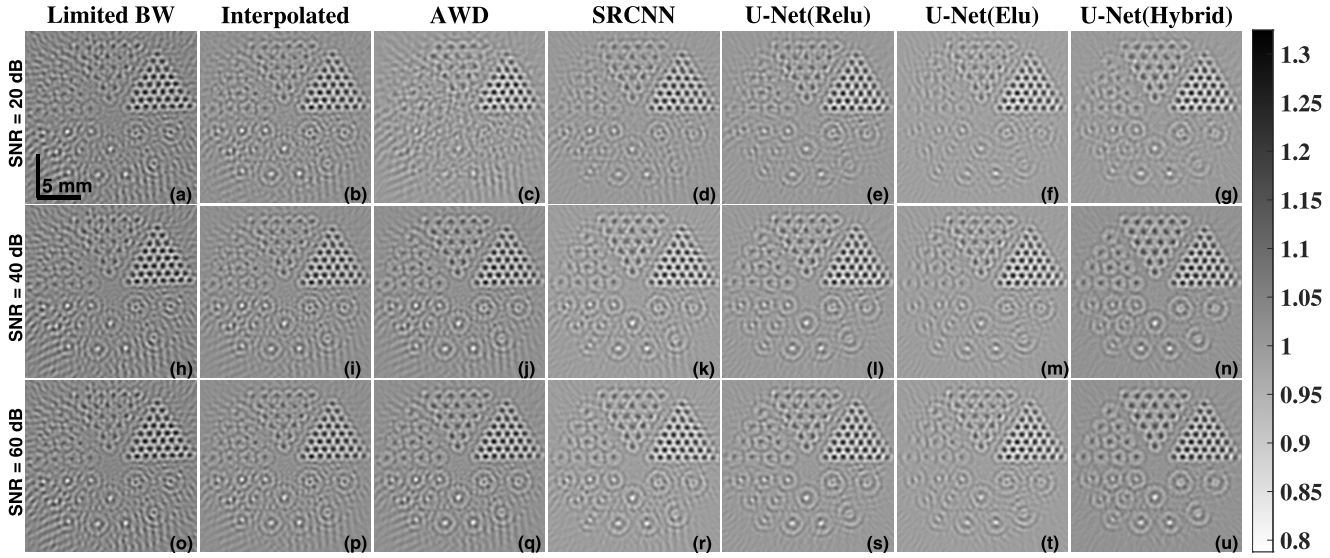

Fig. 5. Reconstructed modified Derenzo phantom images with each row representing the SNR of data being 20, 40, and 60 dB and correspondingly given in (a)–(g), (h)–(n), and (o)–(u), respectively. Reconstructed images using data with limited BW (70%) and 100 transducers are shown in (a), (h), and (o). While (b), (i), and (p) show reconstruction results when the data with 100 transducers that are interpolated using nearest neighbor to obtain a 200 transducer data. (c), (j), and (q) Results obtained using the automated wavelet denoising approach. The results obtained using the SRCNN-based method are shown in (d), (k), and (r), and the results obtained using the U-Net (Relu) are shown in (e), (l), and (s). Finally, (f), (m), and (t) show the results obtained using the proposed U-Net (Elu) approach, and (g), (n), and (u) show the results obtained using the proposed U-Net (Hybrid)-based approach. Table II reports the figure of merits of these results in a comparative manner.

experimental setup and direct the readers to refer to our previous works [75], [76] for elaborate discussions. Note that all experiments conducted on animals were meticulously carried out, adhering to the guidelines and regulations laid out by the Institutional Animal Care & Use Committee of Nanyang Technological University, Singapore (Animal Protocol Number ARF-SBS/NIE-A0263). Section V compares the figures of merits achieved through the proposed method and displays its superiority against state-of-the-art methods along with a visual juxtaposition.

V. RESULTS AND DISCUSSION

In this section, a detailed discussion about the results obtained in terms of the figure of merits is covered. The performance of numerical phantoms has been compared in terms of PC, SSIM, and RMSE, while experimental phantoms are compared based on SNR_r (dB) values. This is followed by the qualitative analysis of the images obtained in both cases. Performance of the proposed approach is compared with both classical and deep-learning-based state-of-the-art techniques and variants of the U-Net architecture. For a fair evaluation, all compared methods were trained using the same data. Note that the proposed scaled-RMSE loss proved crucial in the convergence of all deep-learning-based approaches discussed in this article.

A. Numerical Phantoms

Target images for the PAT phantom (consisting of "PAT" letters), Derenzo (consisting of small and large circles), BV (consisting of thin and thick vessel structures), and Breast phantom (consisting of contrast variations) are shown in Fig. 3(a)–(d), respectively. The image reconstruction obtained

TABLE II
COMPARATIVE RESULTS OBTAINED FOR THE RECONSTRUCTED MODIFIED DERENZO PHANTOM IMAGES SHOWN IN FIG. 5 IN TERMS OF FIGURE OF MERITS: PC COEFFICIENT, SSIM INDEX, AND RMSE FOR SNR OF DATA BEING 20, 40, AND 60 dB. BOLD TEXT INDICATES THE BEST POSSIBLE VALUE FOR THE METRIC USED

SNR	20 dB			40 dB			60 dB		
Method/ Metric	PC	SSIM	RMSE	PC	SSIM	RMSE	PC	SSIM	RMSE
Limited BW	0.3525	0.3199	0.1953	0.3616	0.3263	0.1949	0.3616	0.3263	0.1949
Interpolated	0.6544	0.5425	0.1456	0.6661	0.5610	0.1498	0.6662	0.5612	0.1502
Automated Wavelet Denoising	0.6185	0.5110	0.1177	0.7038	0.5851	0.1426	0.7038	0.5851	0.1426
SRCNN	0.7578	0.6477	0.1103	0.7907	0.6690	**0.0944**	0.7912	0.6697	**0.0940**
U-Net (Relu)	0.7714	0.6707	0.1112	0.8015	0.6900	0.1063	0.8015	0.6905	0.1062
U-Net (Elu)	0.7645	0.6728	**0.0914**	0.7842	0.6833	0.0952	0.7714	0.6707	0.1112
U-Net (Hybrid)	**0.8020**	**0.7015**	0.1031	**0.8305**	**0.7195**	0.1240	**0.8305**	**0.7199**	0.1242

using 200 detectors and full BW is shown in Fig. 3(e)–(h), respectively. These images serve as the desired output for our simulations after the reconstruction is performed using the LBP-based method.

The reconstruction obtained using limited data for the "PAT" phantom using 100 detectors (to serve as limited data case) is shown in Fig. 4(a). The reconstruction obtained after interpolation and then denoising are shown in Fig. 4(b) and (c), respectively, for the "PAT" phantom with SNR of data being 20 dB. The reconstruction obtained for the "PAT" phantom using 200 detectors data using SRCNN is shown in Fig. 4(d), U-Net (Relu) is shown in Fig. 4(e), U-Net (Elu) is shown in Fig. 4(f), and the proposed model U-Net (Hybrid) is shown in Fig. 4(g). The improvements obtained in PC, SSIM, and RMSE compared with the interpolated data case are 35.62%, 30.84%, and 21.09%, respectively, in this case of SNR of data being 20 dB. As seen from the Fig. 4(g), the reconstructed image is relatively artifact free with lesser noise in the background. Similarly, the reconstructions obtained for SNR of data being 40 dB for the limited data, interpolated, denoised, SRCNN, U-Net (Relu), U-Net (Elu), and the proposed technique are shown in Fig. 4(h)–(n), respectively. The improvements obtained in the PC, SSIM, and RMSE was 21.26%, 33.81%, and 29.54%, respectively. As observed in earlier case, the background noise was suppressed to provide improved reconstructed image. Similarly, the reconstructions obtained for the case of SNR of data being 60 dB for the discussed methods are shown in Fig. 4(o)–(u), respectively. The improvements obtained in the PC, SSIM, and RMSE were 21.36%, 33.72%, and 29.54%, respectively.

The reconstruction obtained using the limited data for the Derenzo phantom using 100 detectors is shown in Fig. 5(a). The reconstructions obtained after interpolation and then denoising are shown in Fig. 5(b) and (c), respectively, for the Derenzo phantom with SNR of data being 20 dB. The reconstruction obtained for the Derenzo phantom using 200 detectors data using SRCNN is shown in Fig. 5(d), U-Net (Relu) is shown in Fig. 5(e), U-Net (Elu) is shown in Fig. 5(f), and the proposed model U-Net (Hybrid) is shown in Fig. 5(g) for this case of SNR being 20 dB. The improvements obtained in PC, SSIM, and RMSE compared with the interpolated data case are 22.55%, 29.30%, and 12.40%, respectively. The improvement was similar to the case of "PAT" phantom. Similarly, the reconstructions obtained for the case of SNR of data being 40 dB, interpolated, denoised, SRCNN, U-Net (Relu), U-Net (Elu), and the proposed technique are shown in Fig. 5(h)–(n), respectively. The improvements obtained in the PC, SSIM, and RMSE were 18.00%, 22.97%, and 13.04%, respectively. Similarly, the reconstructions obtained for SNR of data being 60 dB for the discussed methods in this work are shown in Fig. 5(o)–(u), respectively. The improvements obtained in the PC, SSIM, and RMSE were 18.00%, 23.03%, and 12.90%, respectively. The background streak artifact reduction was well achieved using the proposed model compared with other methods.

The reconstruction obtained using the limited data for the BV phantom using 100 detectors is shown in Fig. 6(a). The reconstructions obtained after interpolation and then denoising are shown in Fig. 6(b) and (c), respectively, for the BV phantom for the case of SNR of data being 20 dB. The reconstruction obtained for the BV phantom using 200 detectors data using SRCNN is shown in Fig. 6(d), U-Net (Relu) is shown in Fig. 6(e), U-Net (Elu) is shown in Fig. 6(f), and the proposed model U-Net (Hybrid) is shown in Fig. 6(g) for the case of SNR of data being 20 dB. The improvements obtained in PC, SSIM, and RMSE compared with the interpolated data case are 23.83%, 30.25%, and −3.46%, respectively. Similarly, the reconstructed PA images obtained with SNR of data being 40 dB, interpolated, denoised, SRCNN, U-Net (Relu), U-Net (Elu), and the proposed technique are shown in Fig. 6(h)–(n), respectively. The improvements obtained in the PC, SSIM, and RMSE were 20.96%, 26.11%, and 5.98%, respectively. The reconstructions obtained for SNR of data being 60 dB for the compared techniques are shown in Fig. 6(o)–(u), respectively. The improvements obtained in the PC, SSIM, and RMSE were 21.13%, 26.36%, and 8.41%, respectively.

Finally, complex PA data with variable contrast and noise were used to test the ability of the proposed approach to generalize and adapt to the dynamic environment of any experimental setup. The reconstruction obtained using the limited data for the breast phantom using 100 detectors is shown in Fig. 7(a). The reconstructions obtained after interpolation and

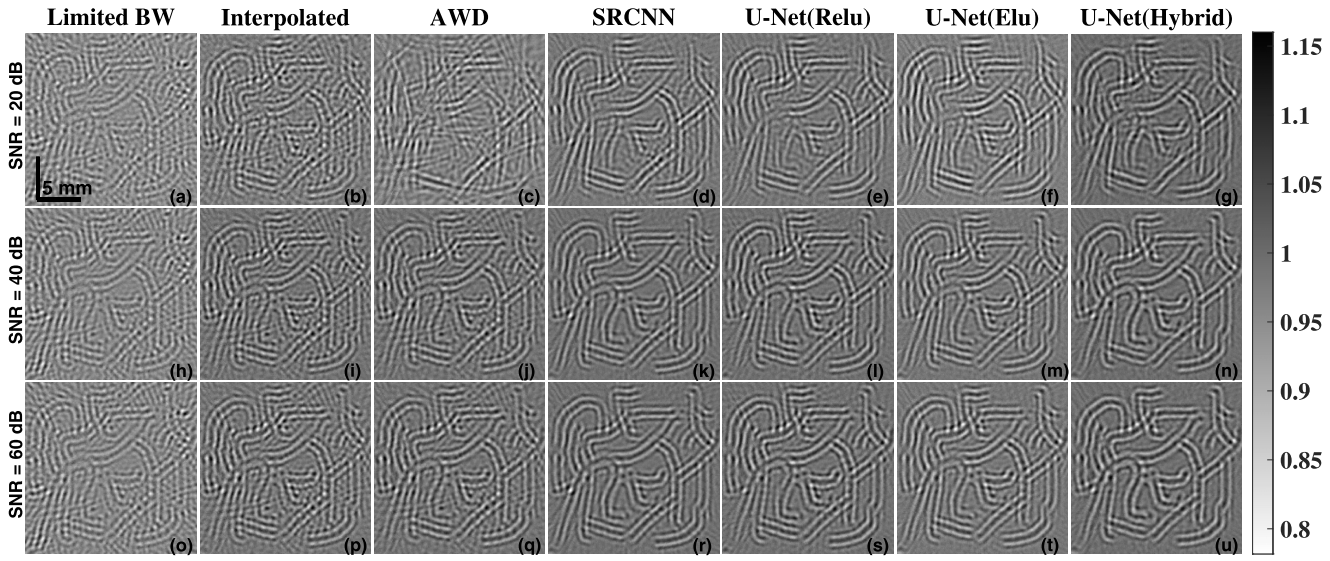

Fig. 6. Reconstructed BV images with each row representing the SNR of data being 20, 40, and 60 dB and correspondingly given in (a)–(g), (h)–(n), and (o)–(u), respectively. Reconstructed images using data with limited BW (70%) and 100 transducers are shown in (a), (h), and (o). While (b), (i), and (p) show the reconstruction results when the data with 100 transducers that are interpolated using nearest neighbor to obtain a 200 transducer data. (c), (j), and (q) Results obtained using the automated wavelet denoising approach. The results obtained using the SRCNN-based method are shown in (d), (k), and (r), and the results obtained using the U-Net (Relu) are shown in (e), (l), and (s). Finally, (f), (m), and (t) show results obtained using the proposed U-Net (Elu) approach, and (g), (n), and (u) show the results obtained using the proposed U-Net (Hybrid)-based approach. Table III reports the figure of merits of these results in a comparative manner.

TABLE III
COMPARATIVE RESULTS OBTAINED FOR THE RECONSTRUCTED BV PHANTOM IMAGES SHOWN IN FIG. 6 IN TERMS OF FIGURE OF MERITS: PC COEFFICIENT, SSIM INDEX, AND RMSE FOR SNR OF DATA BEING 20, 40, AND 60 DB. BOLD TEXT INDICATES THE BEST POSSIBLE VALUE FOR THE METRIC USED

SNR	20 dB			40 dB			60 dB		
Method/ Metric	PC	SSIM	RMSE	PC	SSIM	RMSE	PC	SSIM	RMSE
Limited BW	0.3124	0.2930	0.1429	0.3326	0.3136	0.1375	0.3326	0.3136	0.1375
Interpolated	0.5879	0.4591	0.1155	0.6224	0.4943	0.1200	0.6233	0.4958	0.1161
Automated Wavelet Denoising	0.4617	0.3721	0.1264	0.6540	0.5208	0.1153	0.6540	0.5208	0.1153
SRCNN	0.7094	0.5769	0.1016	0.7870	**0.6607**	0.1022	0.7886	**0.6624**	0.1031
U-Net (Relu)	0.7043	0.5767	0.1016	0.7537	0.6191	0.1084	0.7543	0.6208	0.1072
U-Net (Elu)	0.7154	0.5756	**0.0986**	0.7621	0.6369	**0.0943**	0.7628	0.6374	**0.0934**
U-Net (Hybrid)	**0.7328**	**0.5980**	0.1195	**0.7911**	0.6568	0.1084	**0.7922**	0.6581	0.1056

then denoising are shown in Fig. 7(b) and (c), respectively, for the breast phantom corresponding to the case of SNR of data being 20 dB. The reconstruction obtained for this case using 200 detectors data using SRCNN is shown in Fig. 7(d), U-Net (Relu) is shown in Fig. 7(e), U-Net (Elu) is shown in Fig. 7(f), and the proposed model U-Net (Hybrid) is shown in Fig. 7(g). The improvement obtained in PC, SSIM, and RMSE compared with the interpolated data case are 6.46%, 11.11%, and −9.35%, respectively. Similarly, the reconstructions obtained for SNR of data being 40 dB, interpolated, denoised, SRCNN, U-Net (Relu), U-Net (Elu), and the proposed technique are shown in Fig. 7(h)–(n), respectively. The improvements obtained in the PC, SSIM, and RMSE were 9.69%, 16.94%, and 41.07%, respectively. The reconstructions obtained for the case of SNR of data being 60 dB for the discussed methods in this work are shown in Fig. 7(o)–(u), respectively. The improvements obtained in the PC, SSIM, and RMSE was 10.02%, 17.17%, and 40.77%, respectively. Note that U-Net (Relu) [see Fig. 7(e), (l), and (s)] completely fails to model the variable contrast despite being trained using the same data as other models. This reinforces the robustness of ELUs in deep neural networks for PA imaging tasks.

These numerical results indicate that the proposed method was effective in terms of providing good quality PA data and, thus, able to provide superior results compared with the existing classical and deep-learning-based approaches.

B. Experimental Phantoms

The reconstructed PA images obtained for the horse hair phantom are shown in Fig. 8(a). The reconstructed results for the interpolated and the denoised data are shown

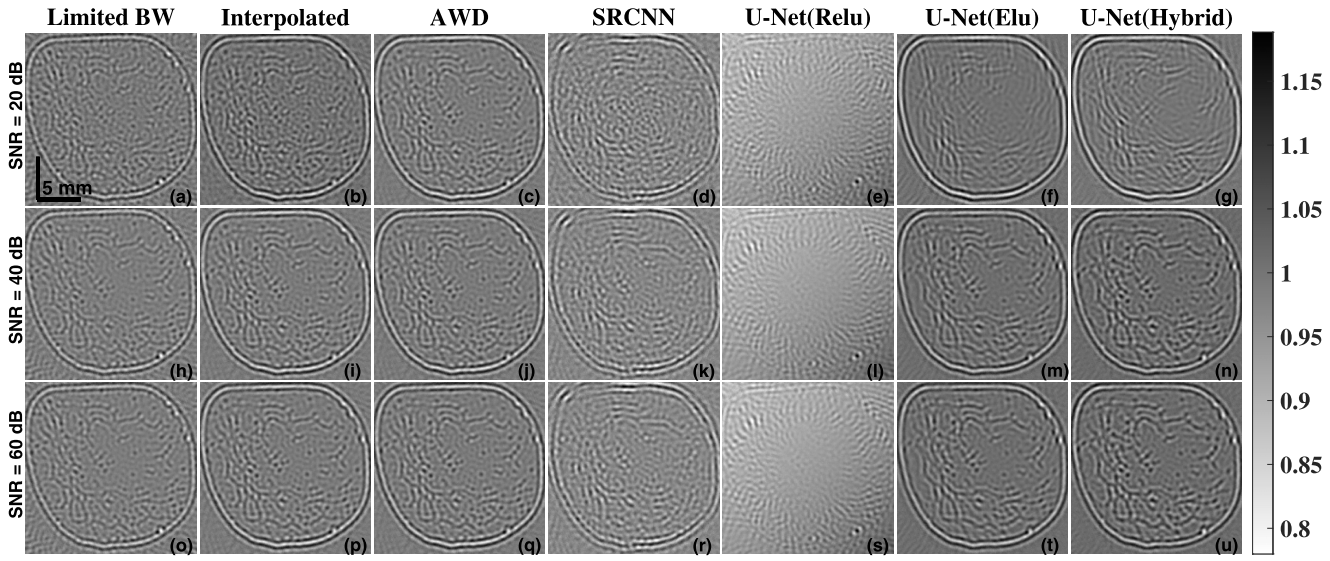

Fig. 7. Reconstructed Breast phantom with each row representing the SNR of data being 20, 40, and 60 dB and correspondingly given in (a)–(g), (h)–(n), and (o)–(u), respectively. Reconstructed images using data with limited BW (70%) and 100 transducers are shown in (a), (h), and (o). While (b), (i), and (p) show the reconstruction results when the data with 100 transducers that are interpolated using nearest neighbor to obtain a 200 transducer data. (c), (j), and (q) Results obtained using the automated wavelet denoising approach. The results obtained using the SRCNN-based method are shown in (d), (k), and (r), and the results obtained using the U-Net (Relu) are shown in (e), (l), and (s). Finally, (f), (m), and (t) show the results obtained using the proposed U-Net (Elu) approach, and (g), (n), and (u) show the results obtained using the proposed U-Net (Hybrid)-based approach. Table IV reports the figure of merits of these results in a comparative manner.

TABLE IV

COMPARATIVE RESULTS OBTAINED FOR THE RECONSTRUCTED BREAST PHANTOM IMAGES SHOWN IN FIG. 7 IN TERMS OF FIGURE OF MERITS: PC COEFFICIENT, SSIM INDEX, AND RMSE FOR SNR OF DATA BEING 20, 40, AND 60 DB. BOLD TEXT INDICATES THE BEST POSSIBLE VALUE FOR THE METRIC USED

SNR	20 dB			40 dB			60 dB		
Method/ Metric	PC	SSIM	RMSE	PC	SSIM	RMSE	PC	SSIM	RMSE
Limited BW	0.5388	0.4287	0.1515	0.5804	0.4858	0.1623	0.5804	0.4858	0.1623
Interpolated	0.7720	0.6208	0.1176	0.8156	0.6874	0.1446	0.8158	0.6877	0.1442
Automated Wavelet Denoising	0.8158	0.6877	0.1442	0.8158	0.6877	0.1442	0.8158	0.6877	0.1442
SRCNN	-0.4389	-0.0619	0.2406	-0.4715	-0.0335	0.2436	-0.4714	-0.0326	0.2460
U-Net (Relu)	-0.0836	0.0787	0.2833	-0.0387	0.1574	0.2835	-0.0372	0.1586	0.2870
U-Net (Elu)	0.8114	**0.7007**	**0.1133**	0.8893	**0.8125**	0.0947	0.8949	**0.8188**	0.0937
U-Net (Hybrid)	**0.8219**	0.6898	0.1286	**0.8947**	0.8039	**0.0852**	**0.8976**	0.8058	**0.0854**

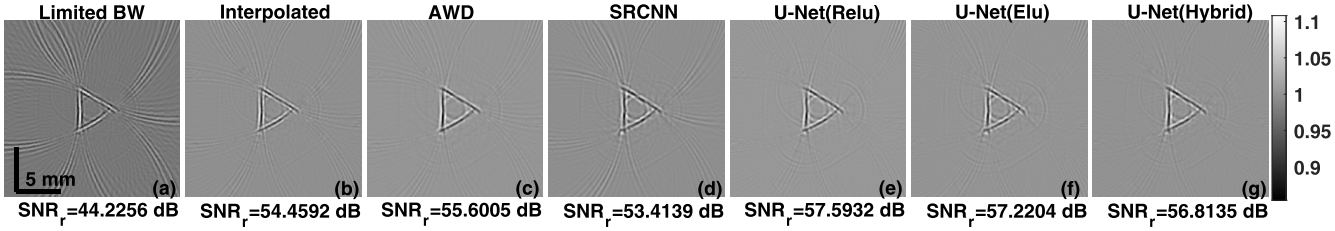

Fig. 8. Reconstructed images for *in vivo* horse hair phantoms for (a) limited BW, 100 transducers, (b) interpolated using nearest neighbor having limited BW but 200 detectors, (c) denoising using automated wavelet approach, (d) SRCNN, (e) U-Net (Relu), (f) proposed U-Net (Elu), and (g) proposed U-Net (Hybrid) approach have been shown. Note that corresponding SNR$_r$ (dB) values have been mentioned below the image.

in Fig. 8(b) and (c), respectively. The reconstructed results obtained using SRCNN is shown in Fig. 8(d), U-Net (Relu) is shown in Fig. 8(e), U-Net (Elu) is shown in Fig. 8(f), and the proposed model U-Net (Hybrid) is shown in Fig. 8(g). The reconstruction obtained using the proposed technique gives a clear background which is free of artifacts compared with the other techniques. The SNR$_r$ is improved compared with the limited BW data reconstruction result by 11.65 dB.

Similar results are obtained for the *in vivo* rat-brain data were shown in Fig. 9(a) for 100 detectors' data. The images

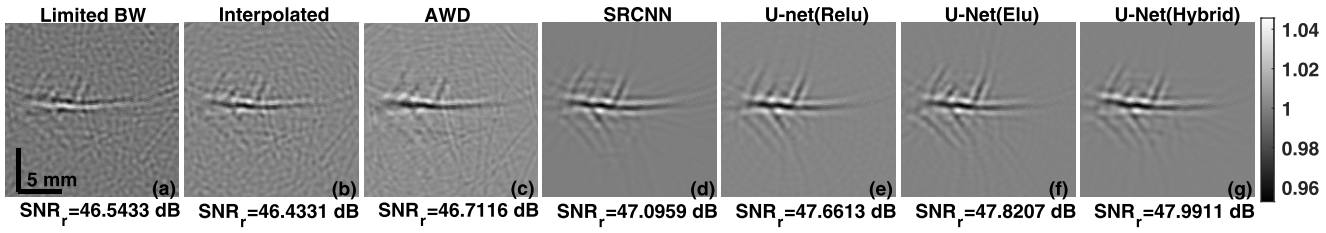

Fig. 9. Reconstructed images for *in vivo* rat-brain data for (a) limited BW, 100 transducers, (b) interpolated using nearest neighbor having limited BW but 200 detectors, (c) denoising using automated wavelet approach, (d) SRCNN, (e) U-Net (Relu), (f) proposed U-Net (Elu), and (g) proposed U-Net (Hybrid) approach have been shown. Note that corresponding SNR$_r$ (dB) values have been mentioned below the image.

obtained using the interpolated and the denoised method are shown in Fig. 9(b) and (c), respectively. The reconstructed results obtained using SRCNN is shown in Fig. 9(d), U-Net (Relu) is shown in Fig. 9(e), U-Net (Elu) is shown in Fig. 9(f), and the proposed model U-Net (Hybrid) is shown in Fig. 9(g). Again, the results obtained using the proposed architecture have shown an artifact-free background, and hence, there is a clear improvement in the image quality. The improvement in SNR$_r$ obtained, compared with the limited data reconstruction, is 1.45 dB.

Note that in this work, the only linear back projection was utilized for characterizing the improvement in data (including BW enhancement, super-resolution, and denoising). It might be possible to utilize the model-based schemes, which can provide further improvement in the reconstructed image quality. As the discussion here is limited to improvement of boundary data using deep learning, only the analytical reconstruction method (linear back projection) was deployed here to reinforce that improvement in the reconstructed image quality is purely due to improvement in the sinogram data.

VI. Conclusion

Deep-learning-based methods have been explored to improve PA imaging, where these methods have been deployed in the image space. This work deploys an U-Net-based architecture for super-resolution and BW enhancement of sinogram data (boundary PA data), and in turn, it provides improved PA image quality. The performance of the proposed network with loss function being scaled RMSE, which is capable of providing much-needed generalization in the PA imaging, was systematically compared in both experimental and numerical scenarios with existing classical and deep-learning-based approaches. The background was free from the streak artifacts, and hence, the superior quality of image reconstruction was obtained. This technique can be applied to other imaging modalities, such as ultrasound tomography, for performing BW enhancement in the data domain. The improvement of image quality due to utilization of the proposed method in the data space in terms of SNR of reconstructed PA image SNR (SNR$_r$) for the *in vivo* phantoms was as high as 11.65 dB compared with the reconstruction obtained using data having limited BW. Methods of the type proposed, which are purely data-driven and having computational complexity being extremely low (for running the trained model), will pave a way for making PA imaging forerunner in the preclinical as well as clinical settings.

References

[1] S. R. Arridge and O. Scherzer, "Imaging from coupled physics," *Inverse Problems*, vol. 28, no. 8, Jul. 2012, Art. no. 080201.

[2] L. V. Wang and S. Hu, "Photoacoustic tomography: *In vivo* imaging from organelles to organs," *Science*, vol. 335, no. 6075, pp. 1458–1462, Mar. 2012.

[3] J. Xia, C. Huang, K. Maslov, M. A. Anastasio, and L. V. Wang, "Enhancement of photoacoustic tomography by ultrasonic computed tomography based on optical excitation of elements of a full-ring transducer array," *Opt. Lett.*, vol. 38, no. 16, pp. 3140–3143, Aug. 2013.

[4] M. Pramanik, G. Ku, C. Li, and L. V. Wang, "Design and evaluation of a novel breast cancer detection system combining both thermoacoustic (TA) and photoacoustic (PA) tomography," *Med. Phys.*, vol. 35, no. 6, pp. 2218–2223, May 2008.

[5] L. V. Wang, "Tutorial on photoacoustic microscopy and computed tomography," *IEEE J. Sel. Topics Quantum Electron.*, vol. 14, no. 1, pp. 171–179, Feb. 2008.

[6] P. K. Upputuri and M. Pramanik, "Recent advances toward preclinical and clinical translation of photoacoustic tomography: A review," *J. Biomed. Opt.*, vol. 22, no. 4, Nov. 2016, Art. no. 041006.

[7] L. Li *et al.*, "Single-impulse panoramic photoacoustic computed tomography of small-animal whole-body dynamics at high spatiotemporal resolution," *Nature Biomed. Eng.*, vol. 1, no. 5, p. 0071, May 2017.

[8] Y. Zhou, J. Yao, and L. V. Wang, "Tutorial on photoacoustic tomography," *J. Biomed. Opt.*, vol. 21, no. 6, Apr. 2016, Art. no. 061007.

[9] J. L. Su *et al.*, "Advances in clinical and biomedical applications of photoacoustic imaging," *Expert Opinion Med. Diag.*, vol. 4, no. 6, pp. 497–510, 2010.

[10] K. Wang, R. Su, A. A. Oraevsky, and M. A. Anastasio, "Investigation of iterative image reconstruction in three-dimensional optoacoustic tomography," *Phys. Med. Biol.*, vol. 57, no. 17, pp. 5399–5423, Aug. 2012.

[11] A. Rosenthal, V. Ntziachristos, and D. Razansky, "Acoustic inversion in optoacoustic tomography: A review," *Current Med. Imag. Rev.*, vol. 9, no. 4, pp. 318–336, Jan. 2014.

[12] C. Huang, K. Wang, L. Nie, L. V. Wang, and M. A. Anastasio, "Full-wave iterative image reconstruction in photoacoustic tomography with acoustically inhomogeneous media," *IEEE Trans. Med. Imag.*, vol. 32, no. 6, pp. 1097–1110, Jun. 2013.

[13] K. Wang, S. A. Ermilov, R. Su, H.-P. Brecht, A. A. Oraevsky, and M. A. Anastasio, "An imaging model incorporating ultrasonic transducer properties for three-dimensional optoacoustic tomography," *IEEE Trans. Med. Imag.*, vol. 30, no. 2, pp. 203–214, Feb. 2011.

[14] Y. Xu, L. V. Wang, G. Ambartsoumian, and P. Kuchment, "Reconstructions in limited-view thermoacoustic tomography," *Med. Phys.*, vol. 31, no. 4, pp. 724–733, Mar. 2004.

[15] S. R. Arridge, M. M. Betcke, B. T. Cox, F. Lucka, and B. E. Treeby, "On the adjoint operator in photoacoustic tomography," *Inverse Problems*, vol. 32, no. 11, Oct. 2016, Art. no. 115012.

[16] S. Arridge *et al.*, "Accelerated high-resolution photoacoustic tomography via compressed sensing," *Phys. Med. Biol.*, vol. 61, no. 24, pp. 8908–8940, Dec. 2016.

[17] N. A. Rejesh, H. Pullagurla, and M. Pramanik, "Deconvolution-based deblurring of reconstructed images in photoacoustic/thermoacoustic tomography," *J. Opt. Soc. Amer. A, Opt. Image Sci.*, vol. 30, no. 10, p. 1994, Sep. 2013.

[18] S. M. Riad, "The deconvolution problem: An overview," *Proc. IEEE*, vol. 74, no. 1, pp. 82–85, Jan. 1986.

[19] M. Cao, T. Feng, J. Yuan, G. Xu, X. Wang, and P. L. Carson, "Spread spectrum photoacoustic tomography with image optimization," *IEEE Trans. Biomed. Circuits Syst.*, vol. 11, no. 2, pp. 411–419, Apr. 2017.

[20] B. Bier *et al.*, "X-ray-transform invariant anatomical landmark detection for pelvic trauma surgery," in *Proc. Int. Conf. Med. Image Comput. Comput.-Assist. Intervent.* Cham, Switzerland: Springer, 2018, pp. 55–63.

[21] M. Aubreville *et al.*, "Deep learning-based detection of motion artifacts in probe-based confocal laser endomicroscopy images," *Int. J. Comput. Assist. Radiol. Surg.*, vol. 14, no. 1, pp. 31–42, Aug. 2018.

[22] A. Akselrod-Ballin, L. Karlinsky, S. Alpert, S. Hasoul, R. Ben-Ari, and E. Barkan, "A region based convolutional network for tumor detection and classification in breast mammography," in *Deep Learning and Data Labeling for Medical Applications*. Cham, Switzerland: Springer, 2016, pp. 197–205.

[23] F.-C. Ghesu *et al.*, "Multi-scale deep reinforcement learning for real-time 3D-landmark detection in CT scans," *IEEE Trans. Pattern Anal. Mach. Intell.*, vol. 41, no. 1, pp. 176–189, Dec. 2017.

[24] H. R. Roth *et al.*, "DeepOrgan: Multi-level deep convolutional networks for automated pancreas segmentation," in *Proc. Int. Conf. Med. Image Comput. Comput.-Assist. Intervent.* Cham, Switzerland: Springer, 2015, pp. 556–564.

[25] P. Moeskops, M. A. Viergever, A. M. Mendrik, L. S. de Vries, M. J. N. L. Benders, and I. Isgum, "Automatic segmentation of MR brain images with a convolutional neural network," *IEEE Trans. Med. Imag.*, vol. 35, no. 5, pp. 1252–1261, May 2016.

[26] S. Chen *et al.*, "Towards automatic abdominal multi-organ segmentation in dual energy CT using cascaded 3D fully convolutional network," 2017, *arXiv:1710.05379*. [Online]. Available: http://arxiv.org/abs/1710.05379

[27] J. J. Nirschl *et al.*, "Deep learning tissue segmentation in cardiac histopathology images," in *Deep Learning for Medical Image Analysis*. Amsterdam, The Netherlands: Elsevier, 2017, pp. 179–195.

[28] G. Wang, J. C. Ye, K. Mueller, and J. A. Fessler, "Image reconstruction is a new frontier of machine learning," *IEEE Trans. Med. Imag.*, vol. 37, no. 6, pp. 1289–1296, Jun. 2018.

[29] M. T. McCann, K. H. Jin, and M. Unser, "Convolutional neural networks for inverse problems in imaging: A review," *IEEE Signal Process. Mag.*, vol. 34, no. 6, pp. 85–95, Nov. 2017.

[30] Z. Zhang, X. Liang, X. Dong, Y. Xie, and G. Cao, "A sparse-view CT reconstruction method based on combination of DenseNet and deconvolution," *IEEE Trans. Med. Imag.*, vol. 37, no. 6, pp. 1407–1417, Jun. 2018.

[31] N. Awasthi, R. Pardasani, S. Kumar Kalva, M. Pramanik, and P. K. Yalavarthy, "Sinogram super-resolution and denoising convolutional neural network (SRCN) for limited data photoacoustic tomography," 2020, *arXiv:2001.06434*. [Online]. Available: http://arxiv.org/abs/2001.06434

[32] S. Antholzer, M. Haltmeier, and J. Schwab, "Deep learning for photoacoustic tomography from sparse data," *Inverse Problems Sci. Eng.*, vol. 27, no. 7, pp. 987–1005, Sep. 2018.

[33] A. Reiter and M. A. Lediju Bell, "A machine learning approach to identifying point source locations in photoacoustic data," *Proc. SPIE*, vol. 10064, Mar. 2017, Art. no. 100643.

[34] D. Allman, A. Reiter, and M. A. L. Bell, "Photoacoustic source detection and reflection artifact removal enabled by deep learning," *IEEE Trans. Med. Imag.*, vol. 37, no. 6, pp. 1464–1477, Jun. 2018.

[35] A. Hauptmann *et al.*, "Model-based learning for accelerated, limited-view 3-D photoacoustic tomography," *IEEE Trans. Med. Imag.*, vol. 37, no. 6, pp. 1382–1393, Jun. 2018.

[36] N. Davoudi, X. L. Deán-Ben, and D. Razansky, "Deep learning optoacoustic tomography with sparse data," *Nature Mach. Intell.*, vol. 1, no. 10, pp. 453–460, Sep. 2019.

[37] H. Lee, J. Lee, and S. Cho, "View-interpolation of sparsely sampled sinogram using convolutional neural network," *Proc. SPIE*, vol. 10133, Feb. 2017, Art. no. 1013328.

[38] H. Lee, J. Lee, H. Kim, B. Cho, and S. Cho, "Deep-neural-network-based sinogram synthesis for sparse-view CT image reconstruction," *IEEE Trans. Radiat. Plasma Med. Sci.*, vol. 3, no. 2, pp. 109–119, Mar. 2019.

[39] J. Kim, J. K. Lee, and K. M. Lee, "Accurate image super-resolution using very deep convolutional networks," in *Proc. IEEE Conf. Comput. Vis. Pattern Recognit. (CVPR)*, Jun. 2016, pp. 1646–1654.

[40] X. Mao, C. Shen, and Y.-B. Yang, "Image restoration using very deep convolutional encoder-decoder networks with symmetric skip connections," in *Proc. Adv. Neural Inf. Process. Syst.*, 2016, pp. 2802–2810.

[41] J. Kim, J. K. Lee, and K. M. Lee, "Deeply-recursive convolutional network for image super-resolution," in *Proc. IEEE Conf. Comput. Vis. Pattern Recognit. (CVPR)*, Jun. 2016, pp. 1637–1645.

[42] C. Ledig *et al.*, "Photo-realistic single image super-resolution using a generative adversarial network," in *Proc. IEEE Conf. Comput. Vis. Pattern Recognit. (CVPR)*, Jul. 2017, pp. 4681–4690.

[43] N. Awasthi, K. R. Prabhakar, S. K. Kalva, M. Pramanik, R. V. Babu, and P. K. Yalavarthy, "PA-fuse: Deep supervised approach for the fusion of photoacoustic images with distinct reconstruction characteristics," *Biomed. Opt. Express*, vol. 10, no. 5, p. 2227, Apr. 2019.

[44] S. Gutta, V. S. Kadimesetty, S. K. Kalva, M. Pramanik, S. Ganapathy, and P. K. Yalavarthy, "Deep neural network-based bandwidth enhancement of photoacoustic data," *J. Biomed. Opt.*, vol. 22, no. 11, Nov. 2017, Art. no. 116001.

[45] C. B. Shaw, J. Prakash, M. Pramanik, and P. K. Yalavarthy, "Least squares QR-based decomposition provides an efficient way of computing optimal regularization parameter in photoacoustic tomography," *J. Biomed. Opt.*, vol. 18, no. 8, Jul. 2013, Art. no. 080501.

[46] N. Awasthi, S. K. Kalva, M. Pramanik, and P. K. Yalavarthy, "Vector extrapolation methods for accelerating iterative reconstruction methods in limited-data photoacoustic tomography," *J. Biomed. Opt.*, vol. 23, no. 4, Feb. 2018, Art. no. 071204.

[47] C. G. A. Hoelen and F. F. M. de Mul, "Image reconstruction for photoacoustic scanning of tissue structures," *Appl. Opt.*, vol. 39, no. 31, pp. 5872–5883, Nov. 2000.

[48] D. B. Percival and A. T. Walden, *Wavelet Methods for Time Series Analysis*, vol. 4. Cambridge, U.K.: Cambridge Univ. Press, 2006.

[49] S. H. Holan and J. A. Viator, "Automated wavelet denoising of photoacoustic signals for circulating melanoma cell detection and burn image reconstruction," *Phys. Med. Biol.*, vol. 53, no. 12, p. N227, May 2008.

[50] D. L. Donoho and I. M. Johnstone, "Ideal spatial adaptation by wavelet shrinkage," *Biometrika*, vol. 81, no. 3, pp. 425–455, Sep. 1994.

[51] M. Irani and S. Peleg, "Improving resolution by image registration," *CVGIP, Graph. Models Image Process.*, vol. 53, no. 3, pp. 231–239, May 1991.

[52] G. Freedman and R. Fattal, "Image and video upscaling from local self-examples," *ACM Trans. Graph.*, vol. 30, no. 2, pp. 1–11, Apr. 2011.

[53] D. Glasner, S. Bagon, and M. Irani, "Super-resolution from a single image," in *Proc. IEEE 12th Int. Conf. Comput. Vis.*, Sep. 2009, pp. 349–356.

[54] J. Yang, Z. Lin, and S. Cohen, "Fast image super-resolution based on in-place example regression," in *Proc. IEEE Conf. Comput. Vis. Pattern Recognit.*, Jun. 2013, pp. 1059–1066.

[55] M. Bevilacqua, A. Roumy, C. Guillemot, and M.-L.-A. Morel, "Low-complexity single-image super-resolution based on nonnegative neighbor embedding," in *Proc. Brit. Mach. Vis. Conf.*, 2012, pp. 1–10.

[56] H. Chang, D.-Y. Yeung, and Y. Xiong, "Super-resolution through neighbor embedding," in *Proc. IEEE Comput. Soc. Conf. Comput. Vis. Pattern Recognit. (CVPR)*, vol. 1, Jul. 2004, p. 1.

[57] W. T. Freeman, E. C. Pasztor, and O. T. Carmichael, "Learning low-level vision," *Int. J. Comput. Vis.*, vol. 40, no. 1, pp. 25–47, 2000.

[58] J. Yang, J. Wright, T. Huang, and Y. Ma, "Image super-resolution as sparse representation of raw image patches," in *Proc. IEEE Conf. Comput. Vis. Pattern Recognit.*, Jun. 2008, pp. 1–8.

[59] J. Yang, J. Wright, T. S. Huang, and Y. Ma, "Image super-resolution via sparse representation," *IEEE Trans. Image Process.*, vol. 19, no. 11, pp. 2861–2873, Nov. 2010.

[60] C. Dong, C. C. Loy, K. He, and X. Tang, "Learning a deep convolutional network for image super-resolution," in *Proc. Eur. Conf. Comput. Vis.* Cham, Switzerland: Springer, 2014, pp. 184–199.

[61] O. Ronneberger, P. Fischer, and T. Brox, "U-Net: Convolutional networks for biomedical image segmentation," in *Proc. Int. Conf. Med. Image Comput. Comput.-Assist. Intervent.* Cham, Switzerland: Springer, 2015, pp. 234–241.

[62] D.-A. Clevert, T. Unterthiner, and S. Hochreiter, "Fast and accurate deep network learning by exponential linear units (ELUs)," 2015, *arXiv:1511.07289*. [Online]. Available: http://arxiv.org/abs/1511.07289

[63] Y. Lou, W. Zhou, T. P. Matthews, C. M. Appleton, and M. A. Anastasio, "Generation of anatomically realistic numerical phantoms for photoacoustic and ultrasonic breast imaging," *J. Biomed. Opt.*, vol. 22, no. 4, Jan. 2017, Art. no. 041015.

[64] P. Burgholzer, J. Bauer-Marschallinger, H. Grün, M. Haltmeier, and G. Paltauf, "Temporal back-projection algorithms for photoacoustic tomography with integrating line detectors," *Inverse Problems*, vol. 23, no. 6, pp. S65–S80, Nov. 2007.

[65] P. Micikevicius *et al.*, "Mixed precision training," 2017, *arXiv:1710.03740*. [Online]. Available: http://arxiv.org/abs/1710.03740
[66] N. Gandhi, M. Allard, S. Kim, P. Kazanzides, and M. A. L. Bell, "Photoacoustic-based approach to surgical guidance performed with and without a da vinci robot," *J. Biomed. Opt.*, vol. 22, no. 12, Aug. 2017, Art. no. 121606.
[67] P. P. Pai, A. De, and S. Banerjee, "Accuracy enhancement for noninvasive glucose estimation using dual-wavelength photoacoustic measurements and kernel-based calibration," *IEEE Trans. Instrum. Meas.*, vol. 67, no. 1, pp. 126–136, Jan. 2018.
[68] Z. Wang, A. C. Bovik, H. R. Sheikh, and E. P. Simoncelli, "Image quality assessment: From error visibility to structural similarity," *IEEE Trans. Image Process.*, vol. 13, no. 4, pp. 600–612, Apr. 2004.
[69] S. Guan, A. A. Khan, S. Sikdar, and P. V. Chitnis, "Fully dense UNet for 2-D sparse photoacoustic tomography artifact removal," *IEEE J. Biomed. Health Informat.*, vol. 24, no. 2, pp. 568–576, Feb. 2020.
[70] J. Prakash, A. S. Raju, C. B. Shaw, M. Pramanik, and P. K. Yalavarthy, "Basis pursuit deconvolution for improving model-based reconstructed images in photoacoustic tomography," *Biomed. Opt. Express*, vol. 5, no. 5, pp. 1363–1377, Apr. 2014.
[71] L. Li, L. Zhu, Y. Shen, and L. V. Wang, "Multiview Hilbert transformation in full-ring transducer array-based photoacoustic computed tomography," *J. Biomed. Opt.*, vol. 22, no. 7, Jul. 2017, Art. no. 076017.
[72] N. Awasthi, S. K. Kalva, M. Pramanik, and P. K. Yalavarthy, "Image-guided filtering for improving photoacoustic tomographic image reconstruction," *J. Biomed. Opt.*, vol. 23, no. 9, Jun. 2018, Art. no. 091413.
[73] B. E. Treeby and B. T. Cox, "K-wave: MATLAB toolbox for the simulation and reconstruction of photoacoustic wave fields," *J. Biomed. Opt.*, vol. 15, no. 2, 2010, Art. no. 021314.
[74] Y. Lou, K. Mitsuhashi, C. M. Appleton, A. Oraevsky, and M. A. Anastasio, "Generation of anatomically realistic numerical phantoms for optoacoustic breast imaging," *Proc. SPIE*, vol. 9708, Mar. 2016, Art. no. 97084O.
[75] S. K. Kalva and M. Pramanik, "Experimental validation of tangential resolution improvement in photoacoustic tomography using modified delay-and-sum reconstruction algorithm," *J. Biomed. Opt.*, vol. 21, no. 8, Aug. 2016, Art. no. 086011.
[76] S. K. Kalva, P. K. Upputuri, and M. Pramanik, "High-speed, low-cost, pulsed-laser-diode-based second-generation desktop photoacoustic tomography system," *Opt. Lett.*, vol. 44, no. 1, pp. 81–84, 2019.

Navchetan Awasthi received the B.Tech. degree in electronics and communication engineering from the National Institute of Technology (NIT) at Jalandhar, Jalandhar, India, in 2011, and the M.Tech. degree in computational science and the Ph.D. degree in medical imaging from the Indian Institute of Science (IISc), Bengaluru, India, in 2016 and 2019, respectively.

He is currently a Research Fellow with Massachusetts General Hospital, Boston, MA, USA, and Harvard University, Cambridge, MA, USA. His research interests include inverse problems in biomedical optics, medical image analysis, medical image reconstruction, biomedical signal processing, and deep learning.

Gaurav Jain (Student Member, IEEE) is currently pursuing the B.Tech. degree in computer science and engineering with Delhi Technological University, New Delhi, India.

His current research interests include computer vision, medical imaging, biometrics, and deep-learning applications.

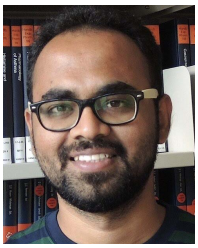

Sandeep Kumar Kalva received the master's degree in biomedical engineering from IIT Hyderabad, Hyderabad, India, in 2015, and the Ph.D. degree in biomedical engineering from Nanyang Technological University, Singapore, in 2019.

He is currently a Postdoctoral Fellow with the University of Zurich, Zürich, Switzerland. His research interests are in optoacoustic imaging and biomedical diagnostics.

Manojit Pramanik received the Ph.D. degree in biomedical engineering from Washington University in St. Louis, St. Louis, MO, USA, in 2010.

He joined the School of Chemical and Biomedical Engineering (SCBE), Nanyang Technological University (NTU), Singapore, in January 2014. His research interests include the development of photoacoustic and thermoacoustic imaging systems, image reconstruction methods, and clinical application areas, such as breast cancer imaging, molecular imaging, contrast agent development, and the Monte Carlo simulation for light transport in biological tissue.

Dr. Pramanik currently serves on the Editorial Board of the *Journal of Biomedical Optics*.

Phaneendra K. Yalavarthy (Senior Member, IEEE) received the M.Sc. degree in engineering from the Indian Institute of Science, Bengaluru, India, in 2004, and the Ph.D. degree in biomedical computation from the Dartmouth College, Hanover, NH, USA, in 2007.

He is currently an Associate Professor with the Department of Computational and Data Sciences, Indian Institute of Science. His research interests include medical image computing, medical image analysis, and biomedical optics.

Dr. Yalavarthy is also a Senior Member of the Society of Photo-Optical Instrumentation Engineers (SPIE) and Optical Society of America (OSA). He also serves as an Associate Editor for the IEEE TRANSACTIONS ON MEDICAL IMAGING.